ACS Sustainable Chemistry & Engineering

Research Article

pubs.acs.org/journal/ascecg

Graphene Quantum Dots-Supported Palladium Nanoparticles for Efficient Electrocatalytic Reduction of Oxygen in Alkaline Media

Christopher P. Deming,[†] Rene Mercado,[†] Vamsi Gadiraju,[‡] Samantha W. Sweeney,[†] Mohammad Khan,[†] and Shaowei Chen*[,†]

[†]Department of Chemistry and Biochemistry, University of California, 1156 High Street, Santa Cruz, California 95064, United States

[‡]The Harker School, 4300 Bucknell Road, San Jose, California 95130, United States

Supporting Information

ABSTRACT: Graphene quantum dots (GQDs)-supported palladium nanoparticles were synthesized by thermolytic reduction of $PdCl_2$ in 1,2-propanediol at 80 °C in the presence of GQDs and then were subject to hydrothermal treatment at an elevated temperature within the range of 140 to 200 °C. Transmission electron microscopic measurements showed a raspberry-like morphology for the samples before and after hydrothermal treatment at temperatures ≤160 °C, where nanoparticles of ca. 8 nm in diameter formed large aggregates in the range of 50 to 100 nm in diameter, and at higher hydrothermal temperatures (180 and 200 °C), chain-like nanostructures were formed instead. X-ray photoelectron and Raman spectroscopic measurements revealed that the GQD structural defects were readily removed by hydrothermal treatments, and the defect concentrations exhibited a clear diminishment with increasing hydrothermal temperature, as indicated by the loss of oxygenated carbons in XPS and a drop in the D to G band ratio in Raman measurements. Voltammetric studies showed apparent electrocatalytic activity toward oxygen reduction, with a volcano-shaped variation of the activity with GQD defect concentration, and the peak activity was observed for the sample prepared at 180 °C with a mass activity of 23.9 A/g_{Pd} and specific activity of 1.08 A/m^2 at +0.9 V vs RHE. This peak activity is attributed to optimal interactions between Pd and GQD where the GQD defects promoted charge transfer from metal to GQDs and hence weakened interactions with oxygenated intermediates, leading to enhanced ORR activity. The corresponding defect concentration was higher than that identified with the platinum counterparts due to the stronger affinity of oxygen to palladium.

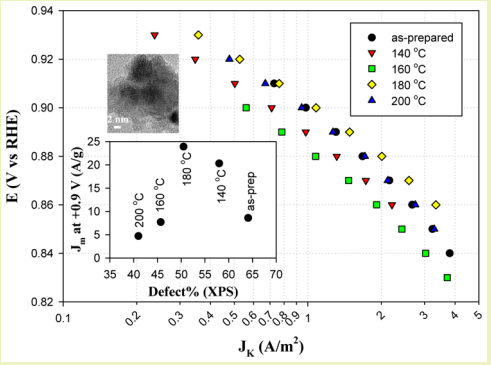

KEYWORDS: *Graphene quantum dot, Palladium nanoparticle, Defect, Hydrothermal, Oxygen reduction, Volcano plot*

INTRODUCTION

Fuel cells, in specific, polymer electrolyte membrane fuel cells (PEMFCs), are currently deemed as a promising source of clean renewable energy for stationary and mobile applications.[1−4] The fast startup and large energy density are optimal for powering large mobile devices, and the ability to stack such fuel cells allows for control over voltage output.[3−5] With water as the only product and numerous sustainable routes to hydrogen generation, hydrogen fuel cells offer much promise to eliminate our dependence on fossil fuels, in addition to reducing greenhouse gas emissions. In fact, cars utilizing PEMFC technologies have demonstrated over 300 miles of travel but have not yet been realized in commercial settings because a large amount of platinum catalysts are needed, even with the large surface area of nanoparticles.[1,6] This is mainly ascribed to the sluggish electron-transfer kinetics and complicated reaction pathways of oxygen reduction reaction (ORR) at the fuel cell cathode.[7,8] Thus, significant research efforts have been devoted to the development of alternative catalysts so as to minimize the use of precious metal catalysts and concurrently improve the ORR activity. In fact, a variety of strategies have been reported, such as controlled growth of particle facets and shapes,[9−12] alloying of metal nanoparticles,[13−16] catalyst size control,[17−20] surface organic functionalization,[21−24] and utilization of new supporting substrates for catalysis.[25−29]

Experimentally, to achieve proper particle dispersion and to limit current losses from catalytic sites to the electrode, metal nanoparticle catalysts are generally supported on a stable, high surface area, conducting material such as the commonly utilized Vulcan supports.[30,31] Yet, as such commercial supports encounter issues with stability and purity, other carbon materials have been examined as effective supporting substrates for fuel cell catalysts, such as mesoporous carbon,[32,33] graphene derivatives (e.g., graphene oxide and GQDs),[28,29] and one-dimensional carbon supports such as carbon nanotubes[34,35] and carbon nanofibers.[27,36] Thus far, graphene derivatives, specifically GQDs, have been widely used and exhibited promising

Received: August 24, 2015
Revised: September 30, 2015
Published: October 21, 2015

DOI: 10.1021/acssuschemeng.5b00927
ACS Sustainable Chem. Eng. 2015, 3, 3315−3323

properties as metal nanoparticle supports due to their chemical inertness, high electrical conductivity, and large surface area.[37−39] More interestingly, these GQD supports have proven to impart electronic interactions with the metal nanoparticles so as to modulate the metal nanoparticle ORR activity.[28,29]

Generally, supports are perceived to play a passive role in providing conduction of currents and dispersion of metal nanoparticles but not significantly influencing the particle electrochemical properties. The idea of electronic interactions between the nanoparticles and supporting materials highlights the main difference between a passive and active support.[40] For instance, GQDs are generally synthesized by chemical oxidation and exfoliation of graphitic precursors, which results in a number of oxygen functional groups on the surface.[41−44] It has been argued that these oxygen defects may result in diminished stability of the graphitic materials through disruption of the sp^2 backbone and are therefore commonly removed through chemical and thermal treatments.[34,45] However, there have been an increasing number of studies where positive contributions are observed from oxygen functional groups on GQDs to metal nanoparticle electrocatalysis.[28,29,35,41] It is proposed that the GQD oxygenated defects provide natural sites for metal particle adhesion allowing for more intimate contacts between particle and support.[35] Additionally, recent DFT studies suggest that the defect groups may pull electrons from the metal nanoparticles, leading to more favorable interactions between the active sites and oxygen intermediates (OIs).[46] In fact, we have observed that GQD-supported Pt nanoparticles (Pt/GQD) exhibited an ORR onset potential 70 mV more positive than similarly sized Pt particles dispersed on commercial carbon supports.[28] The abundance of oxygen groups found on the GQDs are thought to be responsible for the improved activity through diminished electron density on Pt surface atoms and thus improved interactions with OIs. We then identified an optimal defect concentration in a subsequent study where Pt/GQD composites were subject to hydrothermal treatments[47] at temperatures ranging from 140 to 200 °C for 3 to 12 h in order to manipulate the defect concentration. The sample with about 20% structural defects exhibited an activity over 10 times that of samples with too low or too high levels of oxygen defects.[29]

As a platinum group metal, palladium is also a well-studied electrocatalyst for ORR. Because the d-band structure, and hence adsorptive properties, of palladium and platinum are similar, the diverse methods for improving the ORR activity of platinum may also be applicable for palladium.[11,48−50] Numerous reports have indeed detailed the synthesis and characterization of functional nanocomposites based on palladium nanoparticles supported on graphitic materials such as graphene sheets, GQDs, and nanohorns,[51−53] and their ORR activity has been studied.[37,54] However, thus far there has been no systematic study to optimize the ORR activity within the context of GQD defect concentration, to the best of our knowledge. This is the primary motivation of the present study where the goal is to identify optimal conditions for GQD-supported Pd nanoparticles (Pd/GQD) for ORR electrocatalysis. Note that in the volcano plot, palladium binds to OIs more strongly than Pt, thus more substantial electron withdrawing from GQD structural defects is anticipated to achieve marked activity enhancement of the Pd/GQD composites.[48,55] That is, the optimal defect concentration is most likely higher for Pd/GQD than for Pt/GQD.[29]

Experimentally, carbon pitch fibers were thermally and chemically treated in acids to yield stable water-soluble GQDs.[41] Pd/GQD nanocomposites were then synthesized by thermolytic reduction of $PdCl_2$ in 1,2-propanediol in the presence of GQDs and then underwent hydrothermal treatment at controlled temperatures (140 to 200 °C) for 12 h to manipulate the defect concentrations. Since palladium is catalytically active in decarboxylation,[56,57] we should expect a more efficient defect removal than would be at high temperatures alone. The structural details were then characterized by TEM, XPS, and Raman measurements, and the ORR activity was evaluated in alkaline media. Notably, the series of Pd/GQD nanocomposites all exhibited apparent ORR activity, and the activity displayed a clear volcano-shaped variation with the GQD defect concentration. The fact that the GQD defect concentration at the peak ORR activity was higher than that observed for Pt/GQD further confirmed that manipulation of the electronic density of metal nanoparticles by GQD structural defects might be a unique, effective mechanism in enhancing and optimizing the ORR performance.

EXPERIMENTAL SECTION

Chemicals. Palladium(II) chloride ($PdCl_2$, ACROS), pitch carbon fibers (Fiber Glast Development Corporation), sodium hydroxide (NaOH, ≥ 99.5%, Fisher Scientific), sodium carbonate (Na_2CO_3, ≥ 99.5%, Fisher Scientific), hydrochloric acid ($HClO_4$, 70 wt %, ACROS), sulfuric acid (H_2SO_4, Fisher Scientific), nitric acid (HNO_3, Fisher Scientific), and ultrahigh-purity oxygen (99.993%, Praxair) were used as received. Nanopure water was supplied by a Barnstead Nanopure water system (18.3 MΩ cm).

GQD synthesis. The synthesis of GQDs has been detailed previously.[28,29] Experimentally, carbon pitch fibers (1 g) were added to a mixture of concentrated HNO_3 (40 mL) and H_2SO_4 (60 mL) in a round-bottomed flask. Two hours of sonication allowed for proper dispersion of these tightly woven carbon fibers in the acids followed by thermal refluxing at 110 °C for 24 h. When the solution was cooled to room temperature, the solution pH was adjusted to 7 with NaOH. The solution was then left overnight where the supersaturated salts precipitated out of the solution with GQDs dissolved in the water supernatant. The water phase was then loaded into cellulose dialysis bags and placed in Nanopure water for several days to afford purified GQDs that were about 20 nm in diameter and 2 nm in thickness (corresponding to 5−6 layers of graphene sheets, Figure S1). These water-soluble GQDs were then used for the preparation of Pd/GQD nanocomposites, as described below.

Pd/GQD Nanocomposites. $PdCl_2$ (30 mg) was first dissolved in 1 mL of concentrated HCl, and the solution pH was brought to neutral with the addition of Na_2CO_3, followed by centrifugation and removal of residual precipitates. The solution was then added to a flask containing propylene glycol (20 mL) and GQDs prepared above (20 mg) under magnetic stirring. With continuous nitrogen bubbling, the solution was slowly brought to 80 °C and heated at this temperature for 2 h. Complete deposition of palladium on the GQDs was signified by a change in the solution color from dark black to clear and the formation of a dark precipitate at the bottom of the flask. The precipitate was collected and purified with water and underwent centrifugation to remove unreduced palladium and GQDs with little or no metal deposition. The purified samples were referred to as Pd/GQD.

The resulting Pd/GQD nanocomposites were added into 15 mL of water in a Teflon-lined autoclave, which was sealed and hydrothermally treated for 12 h at a controlled temperature of 140, 160, 180, or 200 °C. The resulting particles remained insoluble in water and were denoted as Pd/GQD-T, where T represents the hydrothermal temperature.

Characterization. The morphology and size of the Pd/GQD nanoparticles were characterized by transmission electron microscopic

DOI: 10.1021/acssuschemeng.5b00927
ACS Sustainable Chem. Eng. 2015, 3, 3315−3323

studies (TEM, Philips CM300 at 300 kV). Raman spectroscopic measurements were carried out with a Delta NU 532 nm Raman spectrometer. X-ray photoelectron spectra (XPS) were recorded with a PHI 5400/XPS instrument equipped with an Al Kα source operated at 350 W and 10^{-9} Torr

Electrochemistry. Electrochemical tests were carried out in a standard three-electrode cell connected to a CHI 710C electrochemical workstation, with a Pt foil counter electrode and a reversible hydrogen reference electrode (RHE). The working electrode is a rotating gold ring/glassy-carbon disk electrode (RRDE). A calculated amount of the Pd/GQD nanocomposites prepared above was dispersed in ethanol to prepare a catalyst ink, which was then slowly dropcast onto the glassy-carbon disk electrode of the RRDE and dried under gentle N_2. The catalyst films were then coated with 3 μL of a dilute Nafion solution (0.1 wt %) and dried in air. The catalyst loadings were 20 μg for all samples.

RESULTS AND DISCUSSION

Figure 1 (left panels) depicts a representative TEM micrograph for each of the series of Pd/GQD samples prepared above. It is shown from panel (A) that the as-prepared Pd/GQD composites exhibited a raspberry-like morphology, where a number of small, spherical nanoparticles of ca. 8 nm in diameter clustered together to form large aggregates from 50 to 100 nm. Such behaviors have also been observed with palladium nanoparticles grown on carbon nanoparticles[58] and PdPt nanodendrites.[59] Hydrothermal treatments of the Pd/GQD at 140 and 160 °C did not lead to marked variations of the ensemble morphologies, as depicted in panels (B) and (C). However, at higher hydrothermal temperatures, e.g., 180 °C (panel D) and 200 °C (panel E), individual nanoparticles became increasingly difficult to resolve, and the particles appeared to fuse into much larger agglomerates, forming porous network nanostructures.

The discrepancy of the Pd/GQD nanocomposite structures might be accounted for by the nanoparticle growth dynamics.[60] Chemically produced GQDs are known to include a number of structural defects (i.e., oxygenated groups) that may serve as the anchoring site for metal ion chelation and the growth of metal nanoparticles. Hydrothermal treatment is an effective method in (partially) removing the structural defects and restoring the sp^2 characters.[61,62] Therefore, at higher hydrothermal temperatures, the GQD defects became more effectively removed, leading to less efficient anchoring and passivation of the Pd nanoparticles and hence larger sizes of the metal nanostructures. Further contributions may be ascribed to the Pd nanoparticles formed during the hydrothermal process, which are well-known decarboxylation catalysts,[57] as carboxylic acids have been recognized to be a major oxygenated component of the various oxygenated groups on GQDs (vide infra). This is consistent with the experimental observations. Note that in prior DFT studies it has been found that a hyper cross-linked polystyrene matrix provides unique pockets for palladium nucleation, which are modeled as phenyl groups surrounding the nucleation site, leading to manipulation of the shapes and properties of the Pd nanoparticles.[63] The formation of Pd/GQD likely followed the similar mechanism.

High-resolution TEM studies further confirmed that that $PdCl_2$ was indeed reduced into metallic Pd, forming Pd/GQD nanocomposites. From the respective HRTEM images in Figure 1 (right panels), one can see highly crystalline domains were embedded within a noncrystalline matrix. The former is most likely metallic Pd where the well-defined lattice fringes exhibited an interlayer spacing of 0.23 nm, in good agreement

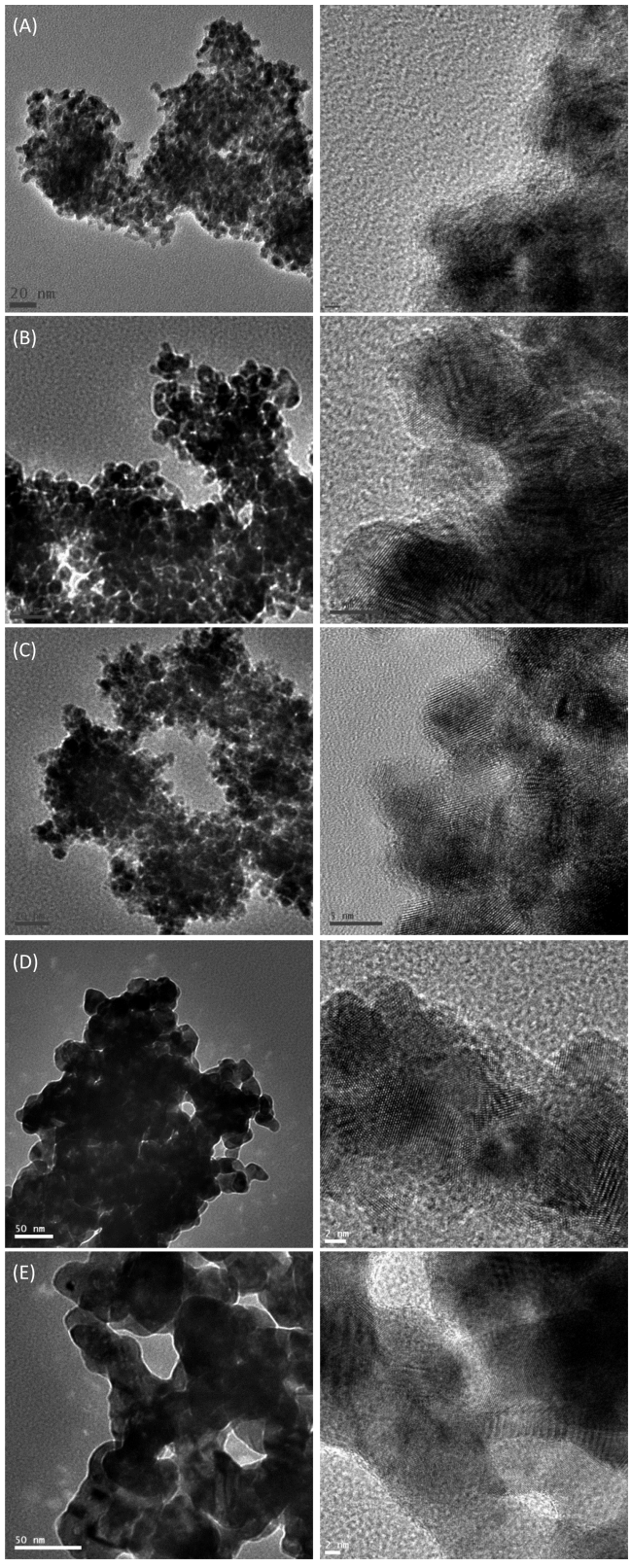

Figure 1. (Left) Representative TEM images of the Pd/GQD nanoparticles (A) before and after hydrothermal treatment at (B) 140 °C, (C) 160 °C, (D) 180 °C, and (E) 200 °C. Scale bars are 20 nm in panels (A) to (C) and 50 nm in (D) and (E). The corresponding high-resolution TEM images are shown in the right panels. Scale bars are 5 nm in panels (A) − (C) and 2 nm in (D) and (E).

DOI: 10.1021/acssuschemeng.5b00927
ACS Sustainable Chem. Eng. 2015, 3, 3315−3323

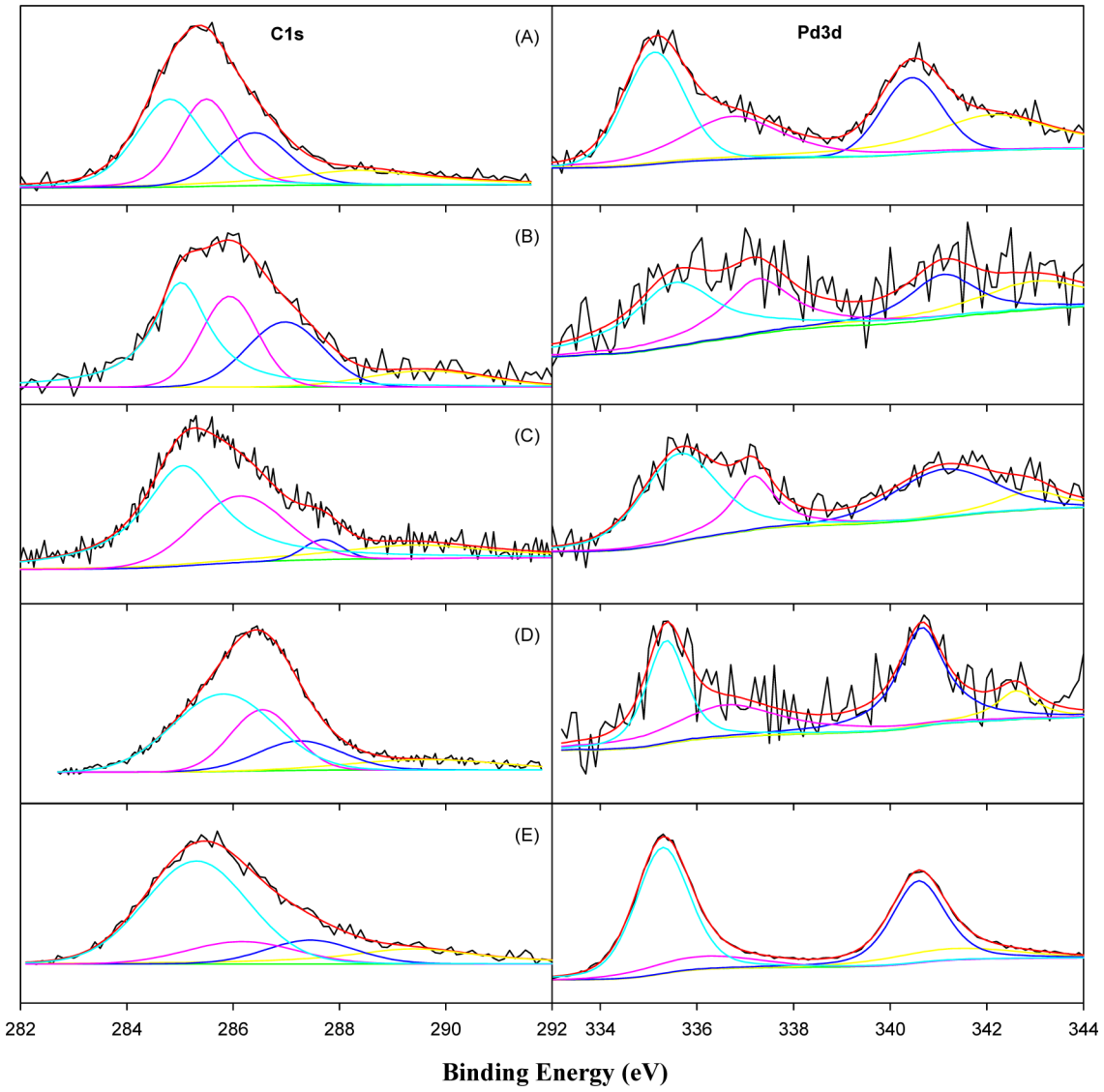

Figure 2. High resolution XPS spectra for the C 1s and Pd 3d electrons for Pd/GQD (A) before and after hydrothermal treatment at (B) 140 °C, (C) 160 °C, (D) 180 °C, and (E) 200 °C. Black curves are experimental data and colored curves are deconvolution fits.

with that of the (111) crystalline planes of *fcc* Pd; whereas the latter may be ascribed to GQDs that were difficult to identify in the TEM images because of their low electron density and poor crystallinity.

Further structural characterization was carried out with XPS measurements. Figure 2 shows the high-resolution scans of the (left panels) C 1s and (right panels) Pd 3d electrons of the Pd/GQD composites before and after hydrothermal treatment at varied temperatures. It is shown from the left panels that deconvolution of the carbon 1s spectra yields four components, graphitic (C═C, 284.8 eV), alcoholic (C−OH, 285.5 eV), carbonylic (C═O, 287.5 eV), and carboxylic (COOH, 288.5 eV). The three oxygen-containing groups can be viewed as structural defects that disrupt the planar graphitic backbone and may be removed to restore the Csp^2 nature.[34,45] On the basis of the integrated peak areas, one can see apparent impacts of hydrothermal temperature on the carbon compositions, where the concentration of oxygenated species decreased with increasing hydrothermal temperature. Specifically, the fraction of oxygenated carbons (i.e., structural defects) in GQDs decreased from 64.1% for the as-prepared sample to 58.0% when treated at 140 °C, 45.7% at 160 °C, 50.5% at 180 °C, and 41.0% at 200 °C (Table 1).

Table 1. Summary of Structural Defects and Compositions in Pd/GQD Nanocomposites

Pd/GQD	Defect %[a]	I_D/I_G[b]	Pd wt %
as-prepared	64.1	1.29	36.7
140 °C	58.0	1.19	17.7
160 °C	45.7	1.01	32.0
180 °C	50.5	1.09	13.1
200 °C	41.0	0.42	66.4

[a]From XPS measurements in Figure 2. [b]From Raman measurements in Figure 3.

Oxygen defects are thought to provide anchoring points for particle attachment but have also been found theoretically[46] and experimentally[28,29] to impart electronic effects on the neighboring metal particles. To reveal the nature of such interactions, high resolution XPS scans of Pd 3d electrons were also acquired and analyzed for each sample. In the right panels

DOI: 10.1021/acssuschemeng.5b00927
ACS Sustainable Chem. Eng. 2015, 3, 3315−3323

of Figure 2, the peaks at ca. 335.0 eV (light blue curve) and 340.5 eV (dark blue curve) may be ascribed to the 3d5/2 and 3d3/2 electrons of metallic palladium, respectively.[64] Peaks colored with pink and yellow represent electron-deficient palladium, which likely results from charge transfer from Pd to electronegative oxygen of the GQDs. As the area of each curve represents the abundance of the corresponding component, it is clear that the hydrothermal temperature had a strong influence on the relative abundance of electron-deficient palladium. In fact, analysis of the XPS data for palladium was very consistent with that for carbon. The as-prepared sample shows the largest relative signal from electron-deficient palladium likely from the high level of oxygen groups in the GQDs. At higher hydrothermal temperatures, the GQD oxygen groups are more effectively removed, leading to diminished signals from electron-deficient palladium. Within the series, Pd/GQD-200 exhibited almost no peaks in the high-energy region, most probably due to the catalytic decarboxylation of GQDs at elevated temperatures.[53,54] In addition, based on the integrated peak areas, the mass fractions of Pd in the nanocomposites were quantitatively estimated to be 36.7% for the as-prepared sample, 17.7% for Pd/GQD-140, 32.0% for Pd/GQD-160, 13.1% for Pd/GQD-180, and 66.4% for Pd/GQD-200 (Table 1).

To further probe the nature of GQD defects, Raman spectroscopy was utilized. Specifically, graphitic materials generally display prominent bands arising from the graphitic (G) and defect (D) domains.[65,66] The intensity ratio of these two bands (I_D/I_G) may be used as a quantitative descriptor for defect concentration. A close-up of the region containing the D and G bands is given in Figure 3 for each sample, and it is

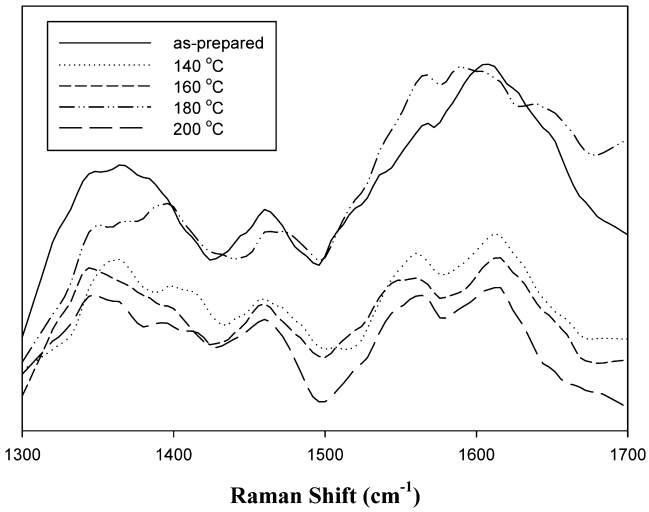

Figure 3. Raman spectra for Pd/GQD nanocomposites before and after hydrothermal treatment at different temperatures (specified in figure legends).

apparent that each sample displays D and G bands at 1385 and 1590 cm^{-1}, respectively (consistent with those of GQDs alone, Figure S2). Furthermore, the I_D/I_G value is strongly dependent on the hydrothermal temperature. For the as-prepared Pd/GQD sample, the I_D/I_G ratio was estimated to be 1.29, which decreased to 1.19 for Pd/GQD-140, 1.01 for Pd/GQD-160, 1.09 for Pd/GQD-180, and 0.42 for Pd/GQD-200 (Table 1), indicating increasingly dominant graphitic characters of the GQDs at increasing hydrothermal temperature. These results are in strong agreement with defect analysis by XPS measurements (Figure 2). Similar behaviors have also been observed in the previous study with Pt/GQD nanocomposites.[29]

Interestingly, the series of Pd/GQD nanocomposites all exhibited apparent electrocatalytic activity toward ORR. A same amount (20 μg) of the Pd/GQD catalysts was dropcast onto a glassy carbon disk for electrochemical evaluations, corresponding to a palladium mass loading of 7.2 μg_{Pd} for Pd/GQD, 3.5 μg_{Pd} for Pd/GQD-140, 6.4 μg_{Pd} for Pd/GQD-160, 2.6 μg_{Pd} for Pd/GQD-180, and 13 μg_{Pd} for Pd/GQD-200, as determined by XPS measurements (Table 1). The electrodes were then subject to electrochemical activation by rapid potential cycling between +0.25 V and +1.6 V at 500 mV/s in a nitrogen-saturated 0.1 M NaOH solution. Figure 4 (A) depicts the

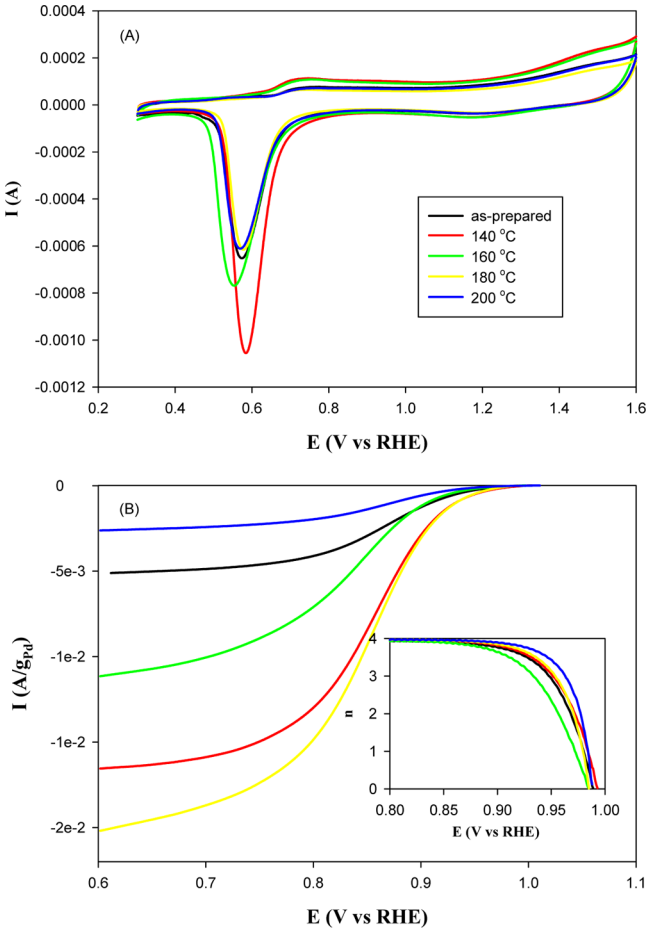

Figure 4. (A) Cyclic voltammograms of a glassy carbon electrode modified with different Pd/GQD nanoparticles in nitrogen-saturated 0.1 M NaOH. Potential sweep rate 100 mV/s. (B) RDE voltammograms of the same electrodes with the electrolyte saturated with oxygen. Inset is the corresponding number of electron transfer during ORR calculated from the RRDE voltammograms at 1600 rpm in Figure S3. Electrode rotation rate 1600 rpm. DC ramp 10 mV/s. Catalyst loading 20 μg.

corresponding steady-state cyclic voltammograms, where the potential range was chosen to avoid the adsorption/absorption/desorption of hydrogen on Pd surfaces. All samples show a voltammetric peak around +0.73 V vs RHE in the anodic scan and a large sharp peak around +0.57 V in the cathodic scan. These represent the formation and removal of an

DOI: 10.1021/acssuschemeng.5b00927
ACS Sustainable Chem. Eng. 2015, 3, 3315−3323

oxide monolayer on the palladium nanoparticle surface, respectively. The electrochemical surface area (ECSA) was then extracted from the integrated charges of the oxide reduction peak at 13.1 m^2/g_{Pd} for the as-prepared Pd/GQD sample, 41.2 m^2/g_{Pd} for Pd/GQD-140, 20.6 m^2/g_{Pd} for Pd/GQD-160, 33.3 m^2/g_{Pd} for Pd/GQD-180, and 7.5 m^2/g_{Pd} for Pd/GQD-200. Of note is that the Pd/GQD-140 sample exhibited the largest ECSA among the series, whereas the Pd/GQD-200 showed the smallest, which might be ascribed to the effective removal of oxygenated defects at high temperatures and hence restacking of the graphene nanosheets that limited the electrochemical accessibility of the Pd surfaces.

The ORR activity of the Pd/GQD samples was then evaluated in oxygen-saturated 0.1 M NaOH. Figure 4 (B) shows the RDE voltammograms of a glassy carbon electrode modified with a calculated amount of the various Pd/GQD nanocomposites at the rotation rates of 1600 rpm. From the figure, it is apparent that each sample displayed a nonzero disk current as the electrode potential was swept in the negative direction, signifying oxygen reduction catalyzed by the Pd/GQD particles. Yet the catalytic performance displayed a marked difference among the Pd/GQD samples. For instance, the onset potential increased in the order of Pd/GQD-160 (+0.86 V) < as-prepared (+0.88 V) < Pd/GQD-140 (+0.89 V) < Pd/GQD-200 ≈ Pd/GQD-180 (+0.90 V). The limiting currents (I_{lim}) also varied markedly. For instance, at the electrode potential of +0.6 V, I_{lim} can be estimated to be 5.15×10^{-3} A/g_{Pd} for as-prepared Pd/GQD, 1.65×10^{-2} A/g_{Pd} for Pd/GQD-140, 1.11×10^{-2} A/g_{Pd} for Pd/GQD-160, 2.02×10^{-2} A/g_{Pd} for Pd/GQD-180, and 2.61×10^{-3} A/g_{Pd} for Pd/GQD-200. These results suggest that the Pd/GQD-180 sample stood out as the best catalyst among the series.

Moreover, the limiting current of the Pd/GQD modified electrodes increased with rotation rate, which was roughly 2 orders of magnitude larger than the ring currents (Figure S3). This signifies a low level of undesired peroxide species produced during oxygen reduction. That is, ORR proceeded largely by the 4-electron reduction pathway. In fact, the numbers of electron transfer (n) in ORR were all close to 4 at potentials more negative than ca. + 0.90 V (inset to Figure 4 (B)), which were quantified by the disk (I_{Disk}) and ring (I_{Ring}) currents, $n = 4I_{Disk}/(I_{Disk} + I_{Ring}/N)$, with N being the collection efficiency of the electrode (40%).[67] Yet a small discrepancy can be seen. For instance, at +0.90 V, n = 3.76 for as-produced Pd/GQD, 3.81 for Pd/GQD-140, 3.64 for Pd/GQD-160, 3.85 for Pd/GQD-180, and 3.89 for Pd/GQD-200.

Further insights into the electron-transfer kinetics were obtained from Koutecky–Levich (K-L) analysis of the RRDE data. Specifically, the disk current may include contributions from both diffusion-controlled (I_d) and kinetic-controlled (I_k) components, as is shown in eq (1)[68]

$$\frac{1}{I_D} = \frac{1}{I_k} + \frac{1}{I_d} = \frac{1}{I_k} + \frac{1}{B\omega^{1/2}} \quad (1a)$$

$$B = 0.62nFAC_O D_O^{2/3} \nu^{-1/6} \quad (1b)$$

$$I_k = nAFkC_O \quad (1c)$$

where ω is the electrode rotation rate, n is electron-transfer number, F is the Faraday constant (96485 C/mol), A is the geometric surface area of the electrode, C_O is the oxygen concentration in O_2-saturated solutions (1.26×10^{-6} mol/cm^3), D_O is the diffusion coefficient of O_2 in 0.1 M NaOH aqueous solution (1.93×10^{-5} cm^2/s), ν is the kinematic viscosity of the solution (1.009×10^{-2} cm^2/s), k is the electron-transfer rate constant. The K-L plots all exhibited good linearity (Figure S4), suggesting first-order reaction of ORR with the oxygen concentration, and from the y intercepts, the kinetic currents (I_k) were quantitatively estimated, which were depicted in the Tafel plot (Figure 5) where the kinetic current

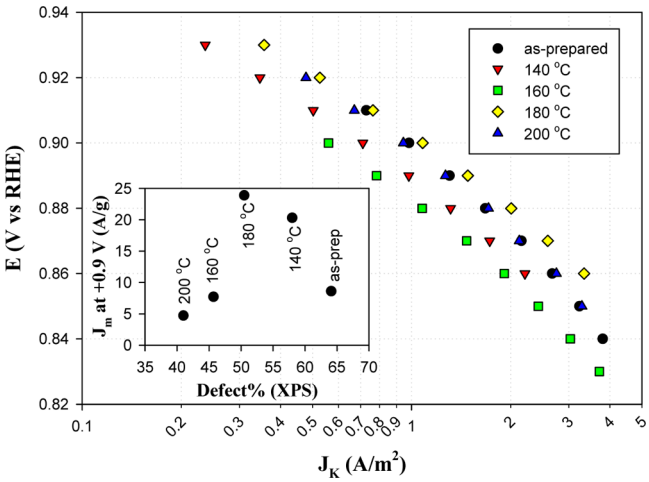

Figure 5. Tafel plot of Pd/GQD nanocomposites in ORR electrocatalysis. Data are obtained from the respective K-L plot in Figure S2. Inset is the mass-specific activity of the various Pd/GQD samples.

density (J_k) was obtained by normalizing I_k to the respective ECSA. One can see that J_k increased markedly with increasingly negative electrode potential, and the Tafel slope varied somewhat among the series of Pd/GQD samples at 96.2 mV/dec for the as-prepared sample, 71.6 mV/dec for Pd/GQD-140, 84.4 mV/dec for Pd/GQD-160, 71.6 mV/dec for Pd/GQD-180, and 82.2 mV/dec for Pd/GQD-200, signifying that the first electron reduction of adsorbed oxygen was likely the rate-determining step for ORR at Pd/GQD.[7] Furthermore, it can be seen that the Pd/GQD-180 sample exhibited the largest J_k at all potentials among the series. For instance, at +0.90 V, J_k = 0.98 A/m^2 for Pd/GQD, 0.71 A/m^2 for Pd/GQD-140, 0.56 A/m^2 for Pd/GQD-160, 1.08 A/m^2 for Pd/GQD-180, and 0.94 A/m^2 for Pd/GQD-200. Mass-specific activity exhibited a similar variation at 8.6 A/g_{Pd} for the as-prepared Pd/GQD, 20.3 A/g_{Pd} for Pd/GQD-140, 7.7 A/g_{Pd} for Pd/GQD-160, 23.9 A/g_{Pd} for Pd/GQD-180, and 4.7 A/g_{Pd} for Pd/GQD-200. From the figure inset, it is shown that the ORR activity actually exhibited a volcano-shaped variation with the GQD structural defects and the Pd/GQD-180 sample represented the optimal interactions between the GQD structural defects and the palladium nanoparticles that led to most favored binding interactions of OIs on Pd surfaces and hence the best ORR performance among the series.

Note that the overall trend is analogous to that observed with the Pt/GQD counterparts; however, the peak ORR performance of the Pd/GQD nanocomposites corresponded to about 50% structural defects within the GQDs (Table 1), which was markedly higher than that (ca. 20%) observed with Pt/GQD.[29] This may be accounted for by the stronger binding interactions of OIs to Pd surfaces than to Pt, as predicted in the volcano plot, such that a higher defect concentration is needed to weaken the interactions of OIs to Pd for maximal ORR activity.[29,45] This is also consistent with previous research on

DOI: 10.1021/acssuschemeng.5b00927
ACS Sustainable Chem. Eng. 2015, 3, 3315−3323

platinum functionalized with electron withdrawing moieties as well as the standing d band theory description of adsorbate−catalyst interactions.[22]

CONCLUSION

In this study, Pd/GQD nanocomposites were synthesized via thermolytic reduction of metal salts in the presence of GQDs and underwent hydrothermal treatment for 12 h at 140, 160, 180, or 200 °C to allow for the controlled removal of oxygen defects and the restoration of the planar Csp^2 backbone. TEM studies showed a raspberry-shaped morphology, which seemed to smooth out as hydrothermal temperature increased as a result of increasing defect removal and thus removal of anchoring points for particle attachment, as indicated by XPS and Raman measurements, which showed good correlation. Voltammetric tests revealed that the defect concentration had a significant impact on the ORR activity with the best sample (Pd/GQD-180) determined on the basis of onset potential, number of electron transfer, specific activity, and mass activity. The peak activity was reached with the optimal level of defects that provided sufficient electron withdrawal from the Pd particles so that the tight binding to OIs was deliberately diminished but would not pull too many electrons away so as to limit the adsorption of oxygen intermediates. The results further confirm the significance of metal−substrate interactions in the manipulation of their electrocatalytic activity, a fundamental insight that may be exploited for the rational design and engineering of nanocomposite catalysts for fuel cell electrochemistry.

ASSOCIATED CONTENT

Supporting Information

The Supporting Information is available free of charge on the ACS Publications website at DOI: 10.1021/acssuschemeng.5b00927.

Representative TEM image, AFM topograph, and Raman spectrum of as-produced GQDs, and additional voltammetric data and analysis. (PDF)

AUTHOR INFORMATION

Corresponding Author

* E-mail: Shaowei@ucsc.edu.

Author Contributions

The manuscript was written through contributions of all authors. All authors have given approval to the final version of the manuscript.

Notes

The authors declare no competing financial interest.

ACKNOWLEDGMENTS

This work was supported in part by the National Science Foundation (CHE-1265635 and DMR-1409396). TEM and XPS work was performed at the National Center for Electron Microscopy and Molecular Foundry, Lawrence Berkeley National Laboratory, as part of a user project.

REFERENCES

(1) Cano-Castillo, U. Hydrogen and fuel cells: Potential elements in the energy transition scenario. *Rev. Mex Fis* **2013**, *59*, 85−92.
(2) Hamrock, S. J.; Herring, A. M.; Zawodzinski, T. A. Fuel cell chemistry and operation. *J. Power Sources* **2007**, *172*, 1.
(3) Dhathathreyan, K. S.; Sridhar, P.; Sasikumar, G.; Ghosh, K. K.; Velayutham, G.; Rajalakshmi, N.; Subramaniam, C. K.; Raja, M.; K, R. Development of polymer electrolyte membrane fuel cell stack. *Int. J. Hydrogen Energy* **1999**, *24*, 1107−1115.
(4) Borup, R.; Meyers, J.; Pivovar, B.; Kim, Y. S.; Mukundan, R.; Garland, N.; Myers, D.; Wilson, M.; Garzon, F.; Wood, D.; Zelenay, P.; More, K.; Stroh, K.; Zawodzinski, T.; Boncella, J.; McGrath, J. E.; Inaba, M.; Miyatake, K.; Hori, M.; Ota, K.; Ogumi, Z.; Miyata, S.; Nishikata, A.; Siroma, Z.; Uchimoto, Y.; Yasuda, K.; Kimijima, K. I.; Iwashita, N. Scientific aspects of polymer electrolyte fuel cell durability and degradation. *Chem. Rev.* **2007**, *107*, 3904−3951.
(5) Wagner, F. T.; Lakshmanan, B.; Mathias, M. F. Elecrochemistry and the Future of the Automobile. *J. Phys. Chem. Lett.* **2010**, *1*, 2204−2219.
(6) Wang, B. Recent development of non-platinum catalysts for oxygen reduction reaction. *J. Power Sources* **2005**, *152*, 1−15.
(7) Song, C.; Zhang, J. *PEM Fuel Cell Electrocatalysis and Catalyst Layers: Fundamentals and Applications* **2008**, 89−134.
(8) Rabis, A.; Rodriguez, P.; Schmidt, T. J. Electrocatalysis for Polymer Electrolyte Fuel Cells: Recent Achievements and Future Challenges. *ACS Catal.* **2012**, *2*, 864−890.
(9) Lee, C.-L.; Chiou, H.-P.; Syu, C.-M.; Wu, C.-C. Silver triangular nanoplates as electrocatalyst for oxygen reduction reaction. *Electrochem. Commun.* **2010**, *12*, 1609−1613.
(10) Ham, D. J.; Phuruangrat, A.; Thongtem, S.; Lee, J. S. Hydrothermal synthesis of monoclinic WO3 nanoplates and nanorods used as an electrocatalyst for hydrogen evolution reactions from water. *Chem. Eng. J.* **2010**, *165*, 365−369.
(11) Shao, M.; Odell, J.; Humbert, M.; Yu, T.; Xia, Y. Electrocatalysis on Shape-Controlled Palladium Nanocrystals: Oxygen Reduction Reaction and Formic Acid Oxidation. *J. Phys. Chem. C* **2013**, *117*, 4172−4180.
(12) Wu, J.; Zhang, J.; Peng, Z. M.; Yang, S. C.; Wagner, F. T.; Yang, H. Truncated Octahedral Pt3Ni Oxygen Reduction Reaction Electrocatalysts. *J. Am. Chem. Soc.* **2010**, *132*, 4984−4985.
(13) Carpenter, M. K.; Moylan, T. E.; Kukreja, R. S.; Atwan, M. H.; Tessema, M. M. Solvothermal synthesis of platinum alloy nanoparticles for oxygen reduction electrocatalysis. *J. Am. Chem. Soc.* **2012**, *134*, 8535−8542.
(14) Seo, A.; Lee, J.; Han, K.; Kim, H. Performance and stability of Pt-based ternary alloy catalysts for PEMFC. *Electrochim. Acta* **2006**, *52*, 1603−1611.
(15) Stamenkovic, V. R.; Mun, B. S.; Arenz, M.; Mayrhofer, K. J. J.; Lucas, C. A.; Wang, G. F.; Ross, P. N.; Markovic, N. M. Trends in electrocatalysis on extended and nanoscale Pt-bimetallic alloy surfaces. *Nat. Mater.* **2007**, *6*, 241−247.
(16) Kitchin, J. R.; Norskov, J. K.; Barteau, M. A.; Chen, J. G. Modification of the surface electronic and chemical properties of Pt(111) by subsurface 3d transition metals. *J. Chem. Phys.* **2004**, *120*, 10240−10246.
(17) Zhou, W. J.; Li, M.; Ding, O. L.; Chan, S. H.; Zhang, L.; Xue, Y. H. Pd particle size effects on oxygen electrochemical reduction. *Int. J. Hydrogen Energy* **2014**, *39*, 6433−6442.
(18) Shao, M. H.; Peles, A.; Shoemaker, K. Electrocatalysis on Platinum Nanoparticles: Particle Size Effect on Oxygen Reduction Reaction Activity. *Nano Lett.* **2011**, *11*, 3714−3719.
(19) Liu, Y.; Zhang, L.; Willis, B. G.; Mustain, W. E. Importance of Particle Size and Distribution in Achieving High-Activity, High-Stability Oxygen Reduction Catalysts. *ACS Catal.* **2015**, *5*, 1560−1567.
(20) Kim, J. W.; Lim, B.; Jang, H. S.; Hwang, S. J.; Yoo, S. J.; Ha, J. S.; Cho, E. A.; Lim, T. H.; Nam, S. W.; Kim, S. K. Size-controlled synthesis of Pt nanoparticles and their electrochemical activities toward oxygen reduction. *Int. J. Hydrogen Energy* **2011**, *36*, 706−712.
(21) Liu, K.; Kang, X.; Zhou, Z.-Y.; Song, Y.; Lee, L. J.; Tian, D.; Chen, S. Platinum nanoparticles functionalized with acetylene derivatives: Electronic conductivity and electrocatalytic activity in oxygen reduction. *J. Electroanal. Chem.* **2013**, *688*, 143−150.

DOI: 10.1021/acssuschemeng.5b00927
ACS Sustainable Chem. Eng. 2015, 3, 3315−3323

(22) Zhou, Z. Y.; Kang, X. W.; Song, Y.; Chen, S. W. Ligand-Mediated Electrocatalytic Activity of Pt Nanoparticles for Oxygen Reduction Reactions. *J. Phys. Chem. C* **2012**, *116*, 10592−10598.
(23) He, G.; Song, Y.; Phebus, B.; Liu, K.; Deming, C. P.; Hu, P.; Chen, S. Electrocatalytic Activity of Organically Functionalized Silver Nanoparticles in Oxygen Reduction. *Sci. Adv. Mater.* **2013**, *5*, 1727−1736.
(24) Pietron, J. J.; Garsany, Y.; Baturina, O.; Swider-Lyons, K. E.; Stroud, R. M.; Ramaker, D. E.; Schull, T. L. Electrochemical Observation of Ligand Effects on Oxygen Reduction at Ligand-Stabilized Pt Nanoparticle Electrocatalysts. *Electrochem. Solid-State Lett.* **2008**, *11*, B161.
(25) Wu, Z. S.; Yang, S. B.; Sun, Y.; Parvez, K.; Feng, X. L.; Mullen, K. 3D Nitrogen-Doped Graphene Aerogel-Supported Fe3O4 Nanoparticles as Efficient Eletrocatalysts for the Oxygen Reduction Reaction. *J. Am. Chem. Soc.* **2012**, *134*, 9082−9085.
(26) Liang, Y. Y.; Li, Y. G.; Wang, H. L.; Zhou, J. G.; Wang, J.; Regier, T.; Dai, H. J. Co3O4 nanocrystals on graphene as a synergistic catalyst for oxygen reduction reaction. *Nat. Mater.* **2011**, *10*, 780−786.
(27) Jia, J. C.; Wang, H.; Ji, S.; Yang, H. J.; Li, X. S.; Wang, R. F. SnO2-embedded worm-like carbon nanofibers supported Pt nanoparticles for oxygen reduction reaction. *Electrochim. Acta* **2014**, *141*, 13−19.
(28) He, G. Q.; Song, Y.; Liu, K.; Walter, A.; Chen, S.; Chen, S. W. Oxygen Reduction Catalyzed by Platinum Nanoparticles Supported on Graphene Quantum Dots. *ACS Catal.* **2013**, *3*, 831−838.
(29) Song, Y.; Chen, S. W. Graphene Quantum-Dot-Supported Platinum Nanoparticles: Defect-Mediated Electrocatalytic Activity in Oxygen Reduction. *ACS Appl. Mater. Interfaces* **2014**, *6*, 14050−14060.
(30) Sharma, S.; Pollet, B. G. Support materials for PEMFC and DMFC electrocatalysts-A review. *J. Power Sources* **2012**, *208*, 96−119.
(31) Zhou, X. J.; Qiao, J. L.; Yang, L.; Zhang, J. J. A review of graphene-based nanostructural materials for both catalyst supports and metal-free catalysts in PEM fuel cell oxygen reduction reactions. *Adv. Energy Mater.* **2014**, *4*.10.1002/aenm.201301523
(32) Joo, S. H.; Kwon, K.; You, D. J.; Pak, C.; Chang, H.; Kim, J. M. Preparation of high loading Pt nanoparticles on ordered mesoporous carbon with a controlled Pt size and its effects on oxygen reduction and methanol oxidation reactions. *Electrochim. Acta* **2009**, *54*, 5746−5753.
(33) Ding, J.; Chan, K. Y.; Ren, J. W.; Xiao, F. S. Platinum and platinum-ruthenium nanoparticles supported on ordered mesoporous carbon and their electrocatalytic performance for fuel cell reactions. *Electrochim. Acta* **2005**, *50*, 3131−3141.
(34) Wang, J. J.; Yin, G. P.; Shao, Y. Y.; Wang, Z. B.; Gao, Y. Z. Investigation of further improvement of platinum catalyst durability with highly graphitized carbon nanotubes support. *J. Phys. Chem. C* **2008**, *112*, 5784−5789.
(35) Hull, R. V.; Li, L.; Xing, Y. C.; Chusuei, C. C. Pt nanoparticle binding on functionalized multiwalled carbon nanotubes. *Chem. Mater.* **2006**, *18*, 1780−1788.
(36) Hsin, Y. L.; Hwang, K. C.; Yeh, C. T. Poly(vinylpyrrolidone)-modified graphite carbon nanofibers as promising supports for PtRu catalysts in direct methanol fuel cells. *J. Am. Chem. Soc.* **2007**, *129*, 9999−10010.
(37) Seo, M. H.; Choi, S. M.; Kim, H. J.; Kim, W. B. The graphene-supported Pd and Pt catalysts for highly active oxygen reduction reaction in an alkaline condition. *Electrochem. Commun.* **2011**, *13*, 182−185.
(38) Geim, A. K.; Novoselov, K. S. The rise of graphene. *Nat. Mater.* **2007**, *6*, 183−191.
(39) Vinayan, B. P.; Nagar, R.; Rajalakshmi, N.; Ramaprabhu, S. Novel Platinum-Cobalt Alloy Nanoparticles Dispersed on Nitrogen-Doped Graphene as a Cathode Electrocatalyst for PEMFC Applications. *Adv. Funct. Mater.* **2012**, *22*, 3519−3526.
(40) Hu, P. G.; Liu, K.; Deming, C. P.; Chen, S. W. Multifunctional graphene-based nanostructures for efficient electrocatalytic reduction of oxygen. *J. Chem. Technol. Biotechnol.* **2015**, *90*, 2132.
(41) He, D. P.; Cheng, K.; Peng, T.; Sun, X. L.; Pan, M.; Mu, S. C. Bifunctional effect of reduced graphene oxides to support active metal nanoparticles for oxygen reduction reaction and stability. *J. Mater. Chem.* **2012**, *22*, 21298−21304.
(42) Li, Y.; Hu, Y.; Zhao, Y.; Shi, G. Q.; Deng, L. E.; Hou, Y. B.; Qu, L. T. An electrochemical avenue to green-luminescent graphene quantum dots as potential electron-acceptors for photovoltaics. *Adv. Mater.* **2011**, *23*, 776−780.
(43) Li, Y.; Zhao, Y.; Cheng, H. H.; Hu, Y.; Shi, G. Q.; Dai, L. M.; Qu, L. T. Nitrogen-Doped Graphene Quantum Dots with Oxygen-Rich Functional Groups. *J. Am. Chem. Soc.* **2012**, *134*, 15−18.
(44) Zhang, Z. P.; Zhang, J.; Chen, N.; Qu, L. T. Graphene quantum dots: an emerging material for energy-related applications and beyond. *Energy Environ. Sci.* **2012**, *5*, 8869−8890.
(45) Li, L.; Xing, Y. C. Electrochemical durability of carbon nanotubes in noncatalyzed and catalyzed oxidations. *J. Electrochem. Soc.* **2006**, *153*, A1823−A1828.
(46) Lim, D. H.; Wilcox, J. Mechanisms of the Oxygen Reduction Reaction on Defective Graphene-Supported Pt Nanoparticles from First-Principles. *J. Phys. Chem. C* **2012**, *116*, 3653−3660.
(47) Tian, L.; Song, Y.; Chang, X. J.; Chen, S. W. Hydrothermally enhanced photoluminescence of carbon nanoparticles. *Scr. Mater.* **2010**, *62*, 883−886.
(48) Lima, F. H. B.; Zhang, J.; Shao, M. H.; Sasaki, K.; Vukmirovic, M. B.; Ticianelli, E. A.; Adzic, R. R. Catalytic Activity-d-Band Center Correlation for the O2 Reduction Reaction on Platinum in Alkaline Solutions. *J. Phys. Chem. C* **2007**, *111*, 404−410.
(49) Hu, G.; Nitze, F.; Gracia-Espino, E.; Ma, J.; Barzegar, H. R.; Sharifi, T.; Jia, X.; Shchukarev, A.; Lu, L.; Ma, C.; Yang, G.; Wagberg, T. Small palladium islands embedded in palladium-tungsten bimetallic nanoparticles form catalytic hotspots for oxygen reduction. *Nat. Commun.* **2014**, *5*, 5253.
(50) Shi, Y.; Yin, S.; Ma, Y.; Lu, D.; Chen, Y.; Tang, Y.; Lu, T. Oleylamine-functionalized palladium nanoparticles with enhanced electrocatalytic activity for the oxygen reduction reaction. *J. Power Sources* **2014**, *246*, 356−360.
(51) Jin, Z.; Nackashi, D.; Lu, W.; Kittrell, C.; Tour, J. M. Decoration, Migration, and Aggregation of Palladium Nanoparticles on Graphene Sheets. *Chem. Mater.* **2010**, *22*, 5695−5699.
(52) Yan, X.; Li, Q.; Li, L. S. Formation and stabilization of palladium nanoparticles on colloidal graphene quantum dots. *J. Am. Chem. Soc.* **2012**, *134*, 16095−16098.
(53) Bekyarova, E.; Hashimoto, A.; Yudasaka, M.; Hattori, Y.; Murata, K.; Kanoh, H.; Kasuya, D.; Iijima, S.; Kaneko, K. Palladium nanoclusters deposited on single-walled carbon nanohorns. *J. Phys. Chem. B* **2005**, *109*, 3711−3714.
(54) Truong-Phuoc, L.; Pham-Huu, C.; Da Costa, V.; Janowska, I. Few-layered graphene-supported palladium as a highly efficient catalyst in oxygen reduction reaction. *Chem. Commun.* **2014**, *50*, 14433−14435.
(55) Norskov, J. K.; Rossmeisl, J.; Logadottir, A.; Lindqvist, L.; Kitchin, J. R.; Bligaard, T.; Jonsson, H. Origin of the Overpotential for Oxygen Reduction at a Fuel-Cell Cathode. *J. Phys. Chem. B* **2004**, *108*, 17886−17892.
(56) Chen, L. M.; Song, Y.; Hu, P. G.; Deming, C. P.; Guo, Y.; Chen, S. W. Interfacial reactivity of ruthenium nanoparticles protected by ferrocenecarboxylates. *Phys. Chem. Chem. Phys.* **2014**, *16*, 18736−18742.
(57) Matsubara, S.; Yokota, Y.; Oshima, K. Palladium-catalyzed decarboxylation and decarbonylation under hydrothermal conditions: Decarboxylative deuteration. *Org. Lett.* **2004**, *6*, 2071−2073.
(58) Huang, J.; Zhou, Z.; Song, Y.; Kang, X. W.; Liu, K.; Zhou, W.; Chen, S. W. Electrocatalytic Activity of Palladium Nanocatalysts Supported on Carbon Nanoparticles in Formic Acid Oxidation. *J. Electrochem* **2012**, *18*, 508−514.
(59) Lim, B.; Jiang, M. J.; Camargo, P. H. C.; Cho, E. C.; Tao, J.; Lu, X. M.; Zhu, Y. M.; Xia, Y. N. Pd-Pt Bimetallic Nanodendrites with High Activity for Oxygen Reduction. *Science* **2009**, *324*, 1302−1305.

DOI: 10.1021/acssuschemeng.5b00927
ACS Sustainable Chem. Eng. 2015, 3, 3315−3323

(60) Chen, S. W.; Templeton, A. C.; Murray, R. W. Monolayer-protected cluster growth dynamics. *Langmuir* **2000**, *16*, 3543−3548.
(61) Zhou, Y.; Bao, Q.; Tang, L. A. L.; Zhong, Y.; Loh, K. P. Hydrothermal Dehydration for the "Green" Reduction of Exfoliated Graphene Oxide to Graphene and Demonstration of Tunable Optical Limiting Properties. *Chem. Mater.* **2009**, *21*, 2950−2956.
(62) Pei, S. F.; Cheng, H. M. The reduction of graphene oxide. *Carbon* **2012**, *50*, 3210−3228.
(63) Prestianni, A.; Ferrante, F.; Sulman, E. M.; Duca, D. Density Functional Theory Investigation on the Nucleation and Growth of Small Palladium Clusters on a Hyper-Cross-Linked Polystyrene Matrix. *J. Phys. Chem. C* **2014**, *118*, 21006−21013.
(64) Wagner, C. D.; Riggs, W. M.; Davis, L. E.; Moulder, J. F.; Muilenberg, G. E. *Handbook of X-ray Photoelectron Spectroscopy: A Reference Book of Standard Data for Use in X-ray Photoelectron Spectroscopy*; Perkin-Elmer Corp.: Eden Prairie, MN, 1979; p x.
(65) Dresselhaus, M. S.; Terrones, M. Carbon-Based Nanomaterials From a Historical Perspective. *Proc. IEEE* **2013**, *101*, 1522−1535.
(66) Ferrari, A. C.; Basko, D. M. Raman spectroscopy as a versatile tool for studying the properties of graphene. *Nat. Nanotechnol.* **2013**, *8*, 235−246.
(67) Zhou, Z. Y.; Kang, X. W.; Song, Y.; Chen, S. W. Enhancement of the electrocatalytic activity of Pt nanoparticles in oxygen reduction by chlorophenyl functionalization. *Chem. Commun.* **2012**, *48*, 3391−3393.
(68) Bard, A. J.; Faulkner, L. R. *Electrochemical Methods: Fundamentals and Applications*, 2nd ed.; John Wiley: New York, 2001.

DOI: 10.1021/acssuschemeng.5b00927
ACS Sustainable Chem. Eng. 2015, 3, 3315−3323